Design and Analysis of the Model Predictive Control Implemented by the ANN Technique for MMC-Based Rectifier With Improved Grid Adaptability

Zheng Gong, *Member, IEEE*, Ping Tuo, Changming Zheng, *Member, IEEE*, and Xiaojie Wu, *Member, IEEE*

***Abstract*—Model predictive control (MPC) has been widely adopted as a modular multilevel converter (MMC)-based active rectifier due to its simplicity, flexibility, and ability to manage multiple control objectives. Nevertheless, the practical implementation of MPC is hindered by the absence of accurate mathematical models. When there are changes in the grid or MMC parameters, the control performance of MPC will deteriorate, indicating weak grid adaptability. For this matter, the employment to implement the MPC by the artificial neural network (ANN) technique is explored to improve the grid adaptability in this article. As ANN is based on data-driven learning, it is not affected by model and grid parameters. More importantly, the strong fault tolerance and generalization of ANN allow it to handle a variety of nonideal grid conditions and different grid impedances, thus improving grid adaptability. Furthermore, the substance regarding why the fault tolerance and generalization of ANN can improve grid adaptability is revealed. In addition, a delay compensation approach for the ANN is proposed to ensure the control performance. Finally, simulation and experiment are performed to verify that the proposed control manner can effectively improve grid adaptability in various grid conditions, including ideal, distorted, unbalanced, and varied impedance grids.**

***Index Terms*—Artificial neural network (ANN), delay compensation, grid adaptability, model predictive control (MPC), modular multilevel converter (MMC).**

I. Introduction

MODULAR multilevel converter (MMC) has become one of the most promising topologies for various medium/high voltage applications owing to its high efficiency, low harmonics, low switching frequency, and highly modularity [1], [2], [3]. As a crucial stage for exchanging energy from ac-side grid to dc-side bus, the MMC-based active rectifier inherits many unique merits of MMC and active rectifier such as permission of four-quadrant operation, lower harmonic characteristics, independent active and reactive power control, etc. [4], [5], [6].

To accomplish the mentioned functions of the MMC-based active rectifier, a safety and reliable control strategy is particularly important. Traditional linear cascaded control strategies, especially proportional integral (PI) or proportional resonant regulators, are widely used in MMC rectifiers to control ac-side current, submodule capacitance voltage, and circulating current, simultaneously [7], [8], [9]. Although linear control can achieve good control effects for MMC rectifiers, its complex structure and parameter design are its biggest drawbacks. Model predictive control (MPC), especially the finite control set MPC (FCS-MPC), has been widely applied in the field of power electronics since its initial introduction. Because of its flexibility, simplicity, and ability to control multiple objectives concurrently, it is especially well-suited for MMC rectifiers, which are multi-input multioutput systems. In addition to having a straightforward and practical design, FCS-MPC also boasts a faster dynamic response and superior THD characteristics [10]. Although FCS-MPC avoids the drawbacks of traditional linear control, it also introduces new problems. By adjusting the weight factor, multiple control objectives can be achieved in one cost function [11], [12]. This will cause multiple control objectives to influence one another, especially the ac-side currents and circulating currents. Moreover, fine-tuning weight factors is a labor-intensive and time-consuming task. To solve this problem, a cascaded FCS-MPC is proposed [13], avoiding the adjustment of weight factors by controlling different variables in different cost functions. Huang et al. [14] and Sun et al. [15] mitigate the adverse effect of circulating current suppression on the ac-side current by using the cascaded FCS-MPC. Zhang et al. [16] follow the same cascaded FCS-MPC concept, with the first stage implementing control of ac-side current and the second stage implementing circulating current suppression based on the first stage, although dual vectors are applied Furthermore, Tuo et al. [17] adopt a three-stage cascaded FCS-MPC. Not only the circulating current is suppressed without adverse effects on the ac-side current, but also the ac-side current is optimized. Nevertheless, the cascaded FCS-MPC does not solve the essential problem of MPC, which is to control based on the mathematical model of MMC rectifiers. Thus, the performance of cascaded FCS-MPC is limited by the accuracy of the model and grid

Manuscript received 28 February 2024; revised 13 May 2024; accepted 26 May 2024. Date of publication 29 May 2024; date of current version 4 September 2024. This work was supported in part by the National Natural Science Foundation of China under Grant 52277205 and Grant 52107217, and in part by the Natural Science Foundation of Jiangsu Province under Grant BK20230108. *(Corresponding author: Zheng Gong.)*

The authors are with the School of Electrical Engineering, China University of Mining and Technology, Xuzhou 221116, China. (e-mail: zgo@cumt.edu.cn; ts21130075a31ld@cumt.edu.cn; changming@cumt.edu.cn; xjwu@cumt.edu.cn).

Color versions of one or more figures in this article are available at https://doi.org/10.1109/TPEL.2024.3406923.

Digital Object Identifier 10.1109/TPEL.2024.3406923

parameters. When the grid is under a nonideal state, or different grid impedance, a deterioration in control performance, or even instability will occur [18], [19], [20].

A growing number of neural networks (NNs) are being used in the field of power electronics as a result of the quick development of digital microprocessors and their increased computational speed [21]. Because of its straightforward structure and simplicity in training, artificial neural network (ANN) has received the most attention among all types of NN [22]. So far, in the field of power electronics, ANN is mainly used to replace MPC to reduce computational complexity [23], [24], [25], improve robustness [22], [25], design weight factors or parameters [26], [27], [28], and extending MMC operation region [28], [29]. Nonetheless, little research has been done on using ANN to increase grid adaptability. ANN can be used to increase grid flexibility due to its fault tolerance and generalization. Although the literature [19] has enhanced grid adaptability by employing ANN to identify grid impedance online based on MPC, it does not take advantage of the inherent qualities of ANN to improve grid adaptability, and the disadvantages of MPC cannot be avoided. Besides, the fundamental attributes of digital microprocessors result in an unavoidable computational delay, which significantly impairs the control performance of ANN.

To address the above-mentioned issue, in this article, the potential that using the FCS-MPC implemented by the ANN to improve the grid adaptability for MMC-based rectifiers is explored. First, the ANN is trained offline using input–output data from cascaded FCS-MPC under an ideal grid. When collecting data, certain fluctuations are applied to the parameters of the grid and MMC, which may be viewed as introducing noise to the input data. Then, the trained ANN is used as a replacement for cascaded FCS-MPC during online operations under ideal grid, nonideal grid, and varied impedance grids. Different from model-based control techniques, ANN is a data-driven learning approach that treats the controlled system as a black box, training the weights and thresholds based solely on input and output data. Owing to the fault tolerance of ANN, correct results can still be produced even when there are errors or noises in some input data. This means that when there is a change in grid impedance or a fault in the grid causing deviations in parameters such as voltage and current, the fault tolerance of ANN prevents large deviations in control, thereby improving the adaptability of the MMC-based active rectifier to the grid. At the same time, ANN has the ability to generalize, meaning that it can accurately output results when processing new data (data not used in the training data). Combining the fault tolerance of ANN, even when the training data for ANN is only collected from an ideal grid, ANN can still have good control performance under nonideal grids, which opens up possibilities for using ANN to enhance grid adaptability. Furthermore, this article reveals the theoretical basis of using the fault tolerance and generalization of ANN to improve the adaptability of the grid. Also, according to the two-step ahead prediction principle, an ANN delay compensation strategy is proposed to solve the deterioration of control performance caused by the intrinsic computational delay of digital implementations. Finally, the effectiveness and reliability of ANN in enhancing the adaptability of the grid are confirmed through simulation and experimental validation.

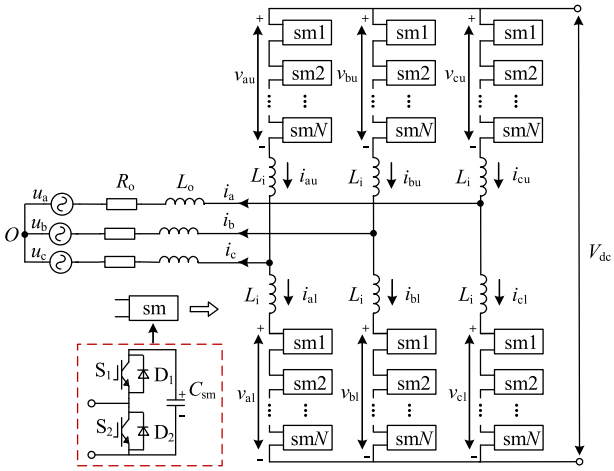

Fig. 1. Diagram of three-phase MMC topology and its submodule.

The rest of this article is organized as follows. In Section II, the basic working principle and mathematical model of the MMC are described and derived. The process of cascaded FCS-MPC is introduced in Section III. Section IV presents the structure of ANN and the detailed process of emulating cascaded FCS-MPC using ANN. Also, the theoretical basis of how ANN improves the adaptability of the grid is briefly described in Section IV. Section V describes the overall control strategy for an MMC-based active rectifier. Section VI shows the simulation and experimental results and Section VII concludes this article.

II. Basic Principle and Mathematical Model of MMC

A. Mathematical Model of MMC

The basic topology of the MMC is shown in Fig. 1, consisting of three phases (a, b, c). Each phase is constructed with an upper arm and a lower arm. Each arm is comprised of N submodules and an arm inductance L_i. Every submodule is a half-bridge structure, composed of two complementary switching devices S_1, S_2, and a submodule capacitor C_{am}. By controlling the switching states of S_1 and S_2, the submodule capacitor C_{sm} can be inserted or bypassed. When S_1 is turned ON and S_2 is turned OFF, the capacitor C_{sm} is inserted; while when S_1 is turned OFF and S_2 is turned ON, the capacitor C_{sm} is in a bypassed state. If the voltage of the submodule capacitors is well balanced, the MMC can output $N+1$ or $2N+1$ phase voltage levels by controlling the state of each submodule. In this article, the $N+1$ phase voltage level is adopted for MMC.

From Kirchhoff's voltage law, the dynamic model of each phase j (j = a, b, c) is

$$v_{ju}(t) = \frac{V_{dc}}{2} - L_i \frac{di_{ju}(t)}{dt} - L_o \frac{di_j(t)}{dt} - R_o i_j(t) - u_j(t) \tag{1}$$

$$v_{jl}(t) = \frac{V_{dc}}{2} - L_i \frac{di_{jl}(t)}{dt} + L_o \frac{di_j(t)}{dt} + R_o i_j(t) + u_j(t) \tag{2}$$

where $V_{\rm dc}$ is the dc-bus voltage, v_{ju} and v_{jl} represent the voltage of the upper arm and lower arm of phase j, i_{ju}, and i_{jl} represent the current of the upper and lower arm of phase j, i_j represents the grid-side current of phase j, and R_o and L_o are the grid side resistance and inductance, respectively.

Similarly, based on Kirchhoff's current law, the grid-side current and circulating current of phase j are as

$$i_j(t) = i_{ju}(t) - i_{jl}(t) \tag{3}$$

$$i_{{\rm diff}j}(t) = \frac{i_{ju}(t) + i_{jl}(t)}{2} = \frac{i_{\rm dc}}{3} + i_{zj}(t) \tag{4}$$

where $i_{\rm dc}$ is the dc-bus current and i_{zj} is the ac component of the circulating current of phase j.

From (1) to (4), the continuous-domain mathematical model of the three-phase grid-side current and the three-phase circulating current can be derived as follows:

$$\frac{{\rm d}i_j(t)}{{\rm d}t} = \frac{1}{L_{\rm i} + 2L_o}(v_{jl}(t) - v_{ju}(t) - 2R_{\rm o}i_j(t) - 2u_j(t)) \tag{5}$$

$$\frac{{\rm d}i_{{\rm diff}j}(t)}{{\rm d}t} = \frac{1}{2L_{\rm i}}(V_{\rm dc} - v_{ju} - v_{jl}). \tag{6}$$

It can be seen from (5) and (6) that both the grid-side current and the circulating current can be controlled by the upper and lower arm voltage. Meanwhile, the continuous-domain model of the submodule capacitor voltage is

$$\frac{{\rm d}u_{{\rm C}rji}(t)}{{\rm d}t} = \frac{i_{rj}(t)}{C_{\rm sm}} \tag{7}$$

where $u_{{\rm C}rji}$ represents the submodule capacitor voltage across the ith ($i = 1, 2, \ldots, N$) of r ($r = u$, l) arm of the phase j.

B. Impact of Unbalanced Grid on MMC

In the case of unbalanced grid conditions, the ac-side voltage can be decomposed into positive-sequence, negative-sequence, and zero-sequence component, and the current will also appear in these three sequence components. Since MMC is usually connected to the ac-side grid via three-phase Y/Δ transformers, there is no zero-sequence voltage and zero-sequence current at the MMC side. Thus, the phase-j ac-side voltage and current can be written as

$$\begin{cases} u_j = U^+\cos(\omega t + \theta_j^+) + U^-\cos\left(\omega t + \theta_j^-\right) \\ i_j = I^+\cos(\omega t + \varphi_j^+) + I^-\cos\left(\omega t + \varphi_j^-\right) \end{cases} \tag{8}$$

where U^+ and U^- are the amplitudes of positive-sequence and negative-sequence ac-side voltages. I^+ and I^- are the amplitudes of positive-sequence and negative-sequence ac-side currents. ${\theta^+}_j$ and ${\theta^-}_j$ are the initial phase angles of positive-sequence and negative-sequence ac-side voltages. ${\varphi^+}_j$ and ${\varphi^-}_j$ are the initial phase angles of positive-sequence and negative-sequence ac-side currents.

The instantaneous power of phase-j is represented by

$$\begin{aligned} p_j(t) &= \left(u_j^+(t) + u_j^-(t)\right)\left(i_j^+(t) + i_j^-(t)\right) \\ &= P_{\rm dc} + p_j^+ + p_j^- + p_j^0 \end{aligned} \tag{9}$$

where $P_{\rm dc}$ represents the dc component of instantaneous power. ${p^+}_j$, ${p^-}_j$, and ${p^0}_j$ represent the positive-sequence, negative-sequence, and zero-sequence of double-line-frequency power ripples, respectively.

By inserting formula (8) into (9), we obtain

$$\begin{cases} p_j^+ = 0.5U^-I^-\cos\left(2\omega t + \theta_j^- + \varphi_j^-\right) \\ p_j^- = 0.5U^+I^+\cos\left(2\omega t + \theta_j^+ + \varphi_j^+\right) \\ p_j^0 = 0.5U^+I^-\cos\left(2\omega t + \theta_j^+ + \varphi_j^-\right) \\ \quad +0.5U^-I^+\cos\left(2\omega t + \theta_j^- + \varphi_j^+\right) \end{cases}. \tag{10}$$

Since the zero-sequence component cannot flow among each phase unit, they cannot be canceled by each other. Therefore, the zero-sequence power will be transmitted to the dc-side, resulting in the presence of a double line-frequency ripple on the dc-side voltage and current [30].

Ignoring the internal losses of MMC, the instantaneous power on the ac-side should be equal to the power on the dc-side. Taking phase-a as an example, it can be concluded that [31]

$$u_j i_j = \frac{U_{\rm dc}}{2} i_{{\rm diff}j}. \tag{11}$$

Substituting (3), (4) and (8) into (11), the ac component of the circulating current can be obtained

$$\begin{aligned} i_{zj} = &\frac{U^-I^-}{U_{\rm dc}}\cos\left(2\omega t + \theta_j^- + \varphi_j^-\right) \\ &+ \frac{U^+I^+}{U_{\rm dc}}\cos\left(2\omega t + \theta_j^+ + \varphi_j^+\right) \\ &+ \frac{U^+I^-}{U_{\rm dc}}\cos\left(2\omega t + \theta_j^+ + \varphi_j^-\right) \\ &+ \frac{U^-I^+}{U_{\rm dc}}\cos\left(2\omega t + \theta_j^- + \varphi_j^+\right). \end{aligned} \tag{12}$$

From (12), it can be seen that in the case of unbalanced grid conditions, there are positive-component, negative-component, and zero-sequence components in the ac component of MMC circulating currents. The components of these three-phase sequences of circulating currents will increase the circulating current, further increasing the power loss of MMC.

III. Principle of Cascaded MPC

A. Discrete Mathematical Model of MMC

Since FCS-MPC is based on discrete mathematical models, it is necessary to discretize the MMC mathematical model by the Euler forward method

$$\frac{{\rm d}x(t)}{{\rm d}t} \approx \frac{x(k+1) - x(k)}{T_{\rm s}} \tag{13}$$

where $x(k+1)$ is the value of x at time step $k+1$, $x(k)$ is the value of x at time step k, and $T_{\rm s}$ is the sampling time.

Applying (13) to (5)–(7), the discrete mathematical model of grid-side current, circulating current, and submodule capacitor voltage at time step $k+1$ can be obtained

$$i_j(k+1) = \frac{T_{\rm s}}{L_{\rm i} + 2L_{\rm o}}[v_{jl}(k+1) - v_{ju}(k+1)]$$

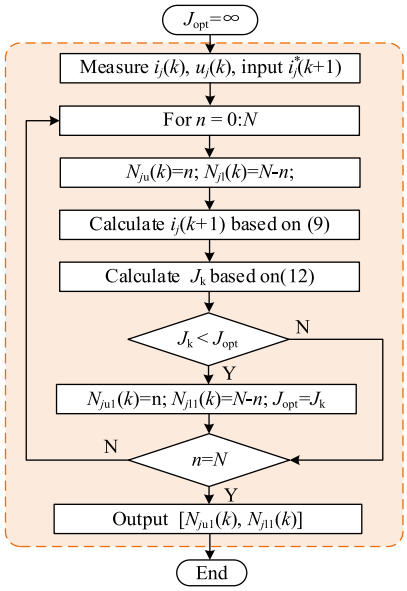

Fig. 2. Control flowchart of grid-side current.

$$+\left(1-\frac{2T_{\mathrm{s}}R_{\mathrm{o}}}{L_{\mathrm{i}}+2L_{\mathrm{o}}}\right)i_j(k)-\frac{2T_{\mathrm{s}}}{L_{\mathrm{i}}+2L_{\mathrm{o}}}u_j(k) \tag{14}$$

$$i_{\mathrm{diff}j}(k+1)=\frac{T_{\mathrm{s}}}{2L_{\mathrm{i}}}[V_{\mathrm{dc}}-v_{j\mathrm{u}}(k+1)-v_{j\mathrm{l}}(k+1)]+i_{\mathrm{diff}j}(k) \tag{15}$$

$$\begin{cases} u_{\mathrm{C}rji}(k+1)=\frac{T_{\mathrm{s}}}{C_{\mathrm{sm}}}i_{rj}(k)+u_{\mathrm{C}rji}(k), S_{rji}(k)=1 \\ u_{\mathrm{C}rji}(k+1)=u_{\mathrm{C}rji}(k), S_{rji}(k)=0 \end{cases} \tag{16}$$

where $i_j(k+1)$ and $i_j(k)$ represent the grid-side current of phase j at time step $k+1$ and k, respectively. $i_{\mathrm{diff}j}(k+1)$ and $i_{\mathrm{diff}j}(k)$ represent the circulating current of phase j at time step $k+1$ and k, respectively. $u_{\mathrm{C}rji}(k+1)$ and $u_{\mathrm{C}rji}(k)$ represent the capacitor voltage of submodule at time step $k+1$ and k, respectively. $S_{rji}(k)$ represents the switching state of the submodule of phase j at time step k.

B. Cascaded FCS-MPC Control Principle for MMC

The cascaded FCS-MPC is mainly divided into two stages. The first stage is grid-side current control. By rolling all possible switching combinations and minimizing the cost function of grid-side current control, the optimum switching combination is selected, namely, the upper arm inserted submodule number $N_{ju1}(k)$ and the lower arm inserted submodule number $N_{jl1}(k)$. If the grid-side reference current at time step $k+1$ is $i_j^*(k+1)$, then the cost function for the first stage is

$$J_{\mathrm{k}}=|i_j^*(k+1)-i_j(k+1)| \tag{17}$$

where $i_j^*(k+1)$ is given by the outer loop. By online rolling optimization, the optimal switching combination $N_{ju1}(k)$ and $N_{jl1}(k)$ for grid-side current control can be obtained by minimizing the cost function J_{k}. The specific optimization process is shown in Fig. 2.

The second stage is the circulating current suppression. On the basis of the first stage, additional δ submodules of upper arm and lower arm are inserted or bypassed based on $N_{ju1}(k)$ and $N_{jl1}(k)$ simultaneously. In this article, the value of δ in simulation is 2 and in the experiment is 1.

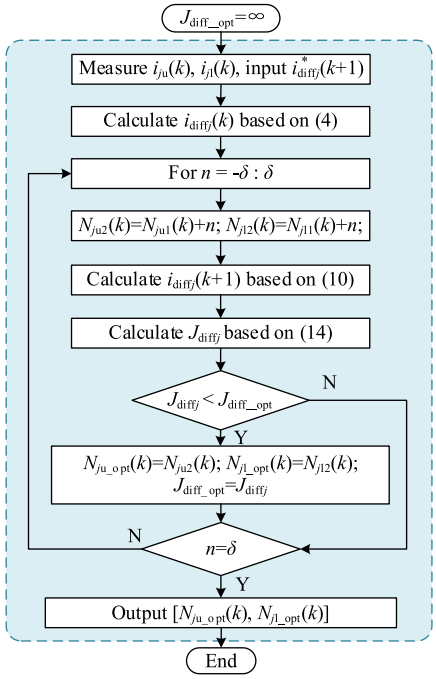

Fig. 3. Control flowchart of circulating current.

According to (4), the circulating current can be divided into dc component and ac component. In order to reduce unnecessary power loss, the ac component should be suppressed. Therefore, the reference value of the circulating current is

$$i_{\mathrm{diff}j}^*=\frac{i_{\mathrm{dc}}}{3}=\frac{P_{\mathrm{AC}}}{3V_{\mathrm{dc}}} \tag{18}$$

where P_{AC} is the active power transmitted by the MMC-based active rectifier system. Therefore, the cost function of the second stage is

$$J_{\mathrm{diff}j}=|i_{\mathrm{diff}j}^*(k+1)-i_{\mathrm{diff}j}(k+1)|. \tag{19}$$

Similarly, by online rolling optimization, minimizing the cost function $J_{\mathrm{diff}j}$, the optimal switching combination for circulating current suppression $N_{j\mathrm{u\_opt}}(k)$ and $N_{j\mathrm{l\_opt}}(k)$ can be obtained. The specific optimization process is shown in Fig. 3.

It is obvious that the second stage, namely, the circulating current suppression is based on the optimal switching state for grid-side current. The optimal switching combination for circulating current suppression $N_{j\mathrm{u\_opt}}(k)$ and $N_{j\mathrm{l\_opt}}(k)$ can be obtained by inserting or bypassing extra submodules based on $N_{ju1}(k)$ and $N_{jl1}(k)$. According to (14), the additional δ submodules of the upper arm and lower arm have no influence on the gird-side current. Therefore, the circulating current suppression stage will not affect the grid-side current.

C. Submodule Capacitor Voltage Control

The voltage of submodule capacitors is balanced using a sorting algorithm. From the second stage of cascaded FCS-MPC,

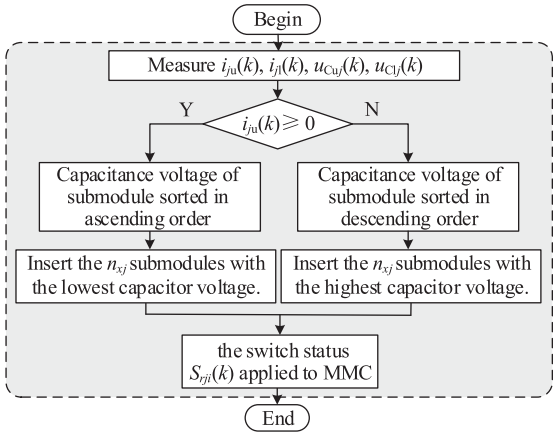

Fig. 4. Flowchart of capacitor voltage sorting algorithm.

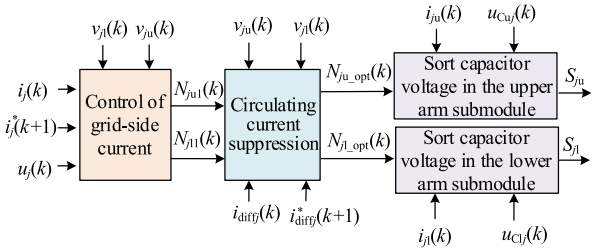

Fig. 5. Overall control block diagram of cascaded FCS-MPC.

it is possible to determine the optimal number of inserted submodules N_{ju_opt} and N_{jl_opt} for the upper and lower arms of MMC. Therefore, based on the direction of the arm current and the sorting results, the submodules are sequentially inserted or bypassed. If the arm current $i_{ju}(k) \geq 0$, the capacitance voltage of the submodule is sorted in ascending order, and the n_{xj} submodules with the lowest capacitor voltage are inserted. At this time, the capacitor is in a charging state; If the arm current $i_{jl}(k) < 0$, the capacitance voltage of the submodule is sorted in descending order, and the n_{xj} submodules with the highest capacitor voltage are inserted. At this time, the capacitor is in a discharge state. Thus, the switching status $S_{rji}(k)$ can be obtained and applied to MMC. The specific flowchart is shown in Fig. 4.

Fig. 5 depicts the comprehensive block diagram of the cascaded FCS-MPC, which encompasses the control of grid-side current, circulating current suppression, and submodule capacitor voltage sorting algorithm. Initially, the grid-side current, grid-side voltage, and submodule capacitance voltage are measured. The reference value of the grid-side current is then input, and the first stage is utilized to fulfill the grid-side current control. This enables the determination of the optimal number of submodules, $N_{ju1}(k)$ and $N_{jl1}(k)$, for grid-side current control. On this premise, the upper arm and lower arm concurrently insert new submodules or bypass additional submodules through the circulating current suppression stage. Hence, with the submodule capacitance voltage sorting approach, the ultimate optimal switching combination $N_{ju\_opt}(k)$ and $N_{jl\_opt}(k)$ is found. At last, the submodule capacitor voltage sorting algorithm produces the switching pulse for the MMC.

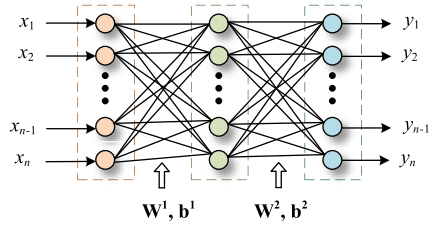

Fig. 6. Basic structure of ANN diagram.

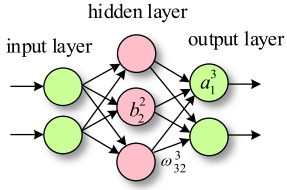

Fig. 7. Simplified structure of ANN.

D. Control Delay Compensation for Cascaded FCS-MPC

Two-step ahead prediction is typically utilized for delay compensation to avoid the degradation of control performance brought by control delay in digital implementations [32]. The core idea of two-step head prediction is to calculate the value of variables at time step $k+1$ according to the optimal switch combination of the previous control period, and then bring it into the mathematical model to predict the value at time step $k+2$. Thus, the output of the minimized cost function is the optimal switch combination at time step $k+2$. According to (14) and (15), the predicted values of grid-side current and circulating current at $k+2$ are as follows:

$$i_j(k+2) = \frac{T_s}{L_i + 2L_o}[v_{jl}(k+2) - v_{ju}(k+2)] + \left(1 - \frac{2T_s R_o}{L_i + 2L_o}\right) i_j(k+1) - \frac{2T_s}{L_i + 2L_o} u_j(k) \tag{20}$$

$$i_{diffj}(k+2) = \frac{T_s}{2L_i}[V_{dc} - v_{ju}(k+2) - v_{jl}(k+2)] + i_{diffj}(k+1). \tag{21}$$

IV. Design of ANN Strategy

A. Basic Principle of ANN

In general, ANN consists of three fundamental layers: the input layer, the hidden layer, and the output layer, as shown in Fig. 6. Each layer consists of several neurons, and there are weights $\mathbf{W}$ and biases $\mathbf{b}$ between each layer. Each neuron of the hidden layer and the output layer has an activation function $g(x)$. The input layer has $\boldsymbol{x}$ inputs and the output layer has $\boldsymbol{y}$ outputs. Here, we take an ANN with two neurons in the input layer, three neurons in the hidden layer, and two neurons in the output layer as an example to illustrate its basic structure and working principle.

As shown in Fig. 7, ω^l_{jk} represents the weight coefficient from the jth neuron in the (l-1)th layer to the kth neuron in the lth layer;

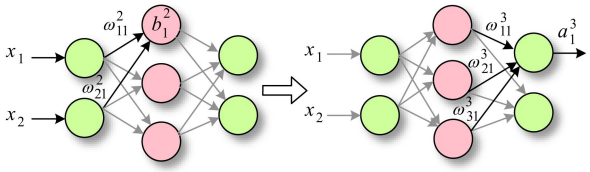

Fig. 8. Principle of forward propagation.

$b^l{}_j$ represents the bias value of the jth neuron in the lth layer; and $a^l{}_j$ represents the output of the jth neuron in the lth layer. Therefore, the output of the jth neuron in the lth layer can be expressed as

$$a_j^l = g\left(\sum_k w_{jk}^l a_k^{l-1} + b_j^l\right) \tag{22}$$

where g represents the activation function, the activation function of the hidden layer neurons in this article is the "*Tanh*" function

$$g(x) = \frac{2}{1+e^{-2x}} - 1. \tag{23}$$

The activation function of the output layer neurons in this article is the "*Purelin*" linear function

$$g(x) = x. \tag{24}$$

It is worth mentioning that the commonly used activation function, in addition to the ones mentioned above, is the "*ReLu*" function, which is expressed as follows:

$$g(x) = \begin{cases} 0, x < 0 \\ x, x \geq 0 \end{cases}. \tag{25}$$

The basic principle of ANN is forward propagation, as shown in Fig. 8. The input of the first neuron in the input layer is x_1. The input of the second neuron in the input layer is x_2. The output of the first neuron in the hidden layer is

$$a_1^2 = \sigma\left(\omega_{11}^2 x_1 + \omega_{21}^2 x_2 + b_1^2\right). \tag{26}$$

Similarly, the output of the second neuron in the hidden layer is

$$a_2^2 = \sigma\left(\omega_{12}^2 x_1 + \omega_{22}^2 x_2 + b_2^2\right). \tag{27}$$

The output of the third neuron in the hidden layer is

$$a_3^2 = \sigma\left(\omega_{13}^2 x_1 + \omega_{23}^2 x_2 + b_3^2\right). \tag{28}$$

As a result, the output of the first neuron in the output layer is

$$a_1^3 = \sigma\left(\omega_{11}^3 a_1^2 + \omega_{21}^3 a_2^2 + \omega_{31}^3 a_3^2 + b_1^3\right). \tag{29}$$

The outputs of the other neurons in the output layer follow the same procedure as described above. Since all ANN outputs are consequently calculated layer by layer in the forward direction, the term "forward propagation" is coined. Therefore, ANN actually is a function of inputs $\boldsymbol{x}$, weights $\mathbf{W}$, and biases $\mathbf{b}$

$$\boldsymbol{y} = \boldsymbol{f}\left(\boldsymbol{W}, \boldsymbol{b}; \boldsymbol{x}\right) \tag{30}$$

or more simply $\boldsymbol{y} = \boldsymbol{f}(\mathbf{s})$, where $\boldsymbol{x} = [x_1, \ldots, x_n]^T$, $\boldsymbol{y} = [y_1, \ldots, y_n]^T$, $\mathbf{W} = [\omega^l{}_{jk}]$, $\mathbf{b} = [b^l{}_j]$ and $\boldsymbol{f} = [f_1, \ldots, f_n]^T$.

B. Training Process of ANN

Technically, the training process of ANN is a process of constantly adjusting the weight coefficients and biases between different layers. As long as there are enough training data and hidden neurons, an ANN may theoretically imitate any input and output properties by altering the weight coefficient and bias. The Backpropagation (BP) algorithm is widely employed as a training method for NNs due to its exceptional accuracy in fitting [33]. The basic principle of the BP algorithm is to use the gradient descent method based on the error function to calculate the error gradient of each neuron in the backward propagation from the output layer and propagate it back to the preceding layer. For each weight and bias, their values are updated according to the gradient direction, learning rate, and error function [34]. The definition of the error function is as follows.

Assuming $\boldsymbol{x}^m$ and $\boldsymbol{y}^m$ ($m = 1, \ldots, M$) are the input and output data that the ANN is required to learn. To achieve a network that generates an output $\boldsymbol{y}^m$ for the input $\boldsymbol{x}^m$, the error function that minimizes the values of $\mathbf{W}$ and $\mathbf{b}$ is given by

$$Q(\boldsymbol{W}, \boldsymbol{b}) = \sum_m \left|\boldsymbol{y}^m - \boldsymbol{f}(\boldsymbol{x}^m)\right|^2 \tag{31}$$

where $|\cdot|$ denotes the Euclidean norm of a vector.

In this article, an NN uses an improved algorithm of the BP algorithm called the Levenberg-Marquardt algorithm, which is represented as "*trainlm*" algorithm in MATLAB Deeping Learning Toolbox. In order to ensure a sufficient amount of data, 35 sets of data are randomly chosen, with 70% being used for training, 15% for testing, and 15% for validation. The testing data is used to track the training regression of the ANN, the training data is used to train it, and the validation data prevents it from over-fitting.

C. Using ANN to Emulate Cascaded FCS-MPC

This article adopts an input layer, hidden layer, and output layer structure when ANN is applied to MMC. The input layer of the ANN is made up of seven neurons because it is used to emulate cascaded FCS-MPC. These neurons represent the grid-side current reference value $i_j^*(k+1)$, upper arm current i_{ju}, lower arm current i_{jl}, upper arm voltage v_{ju}, lower arm voltage v_{jl}, grid-side voltage u_j, and circulating current reference value $i^*{}_{\mathrm{diff}j}$. The output layer consists of two neurons, denoted as n_{uj} and n_{lj}, which correspond to the number of submodules in the upper and lower arms, respectively. In order to ensure that the number of submodules remains an integer, the round function is employed in this context to round off the output. The complete structure is shown in Fig. 9.

In theory, the more hidden layer neurons, the higher the degree of fitting to the original algorithm, but the greater the amount of computation, and vice versa. Six neurons (simulation) and four neurons (experiment) in the hidden layer are selected to ensure the fitting properties and minimize the computational load in

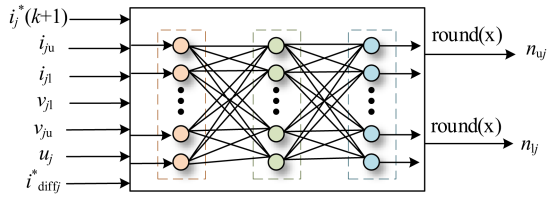

Fig. 9. ANN structure for MMC.

this article. As depicted in Fig. 10, the entire ANN structure for simulating cascaded FCS-MPC to control MMC.

First, the input and output data of cascaded FCS-MPC are collected. Next, gather input and output information for offline ANN training. These data are used to train the ANN offline, making the input and output properties essentially consistent with cascaded FCS-MPC. Finally, cascaded FCS-MPC will be replaced online by a trained ANN.

It is worth pointing out that all training data of ANN in this article are input-output data of cascaded FCS-MPC under ideal grid conditions. However, the ANN trained on data based on ideal grid conditions still performs well under nonideal grid and grid impedance variation conditions. This is because of the fault tolerance and generalization properties of ANN. The specific theoretical basis will be presented in Section IV-E.

D. Control Delay Compensation for ANN

The delay compensation strategy of cascaded FCS-MPC is a two-step ahead prediction. The anticipated value of the control variable at time step $k+2$ is calculated in accordance with the switching combination of the prior control period, and the best switching combination is then achieved by minimizing the value function. In essence, the switching combination of the previous control period (time step $k+1$) is used as the input of the next control period (time step $k+2$) to predict. The delay compensation strategy for ANN operates in a similar manner, using the switching combination from the preceding control period as its input.

Therefore, a total of nine neurons make up the input layer of the ANN with delay compensation strategy, and in addition to the seven control variables described above, it additionally requires the inserted submodule numbers $n_{\mathrm{u}j}(k\text{-}1)$ and $n_{\mathrm{l}j}(k\text{-}1)$ of the upper and lower arms of the previous control period. Fig. 11 depicts the ANN structure with a delay compensation strategy.

E. Theoretical Basis for Improving Grid Adaptability by ANN

The ability of ANN to improve grid adaptability mainly comes from two inherent characteristics, namely fault-tolerance and generalization. The following will discuss these two characteristics of ANN separately.

1) Fault-Tolerance: Taking the nonlinear system sgn (ReLu (x)) as an example, where sgn(x) is

$$\operatorname{sgn} x = \begin{cases} 1, x > 0 \\ 0, x = 0 \\ -1, x < 0 \end{cases}. \tag{32}$$

If an input x is distributed according to a Bernoulli distribution with a probability parameter of $p = 0.5$ and is combined with noise $\varepsilon \sim M$ (0,1), then the resulting noisy input has a 50% probability of not influencing the output computed by sgn (*ReLu* (x)). This demonstrates the property of fault tolerance. In this fault tolerance example, it is evident that the data x follows a nonidentically distributed, independent random noise ε, and that the nonlinear system helps to filter out the noise. The situation where the data has a different distribution from the noise is almost inevitable in the input of ANN. Moreover, ANN typically contains a large number of such nonlinear processes, or "nonlinear filters" [35]. Therefore, ANN itself is a superior nonlinear filter. In practice, when the grid encounters some nonideal states or different grid impedance, ANN can filter out the perturbed data and noise, and obtain accurate output results, providing excellent fault tolerance and robustness. Consequently, it is possible to enhance grid adaptability of MMC by leveraging the fault tolerance of ANN.

2) Generalization: The generalization ability of ANN refers to its ability to adapt to new samples, that is, its ability to approximate the target value of a given input that is not included in the training set. The above-mentioned principle is formulated mathematically as follows [36].

Assuming $\hat{\boldsymbol{x}}^m$ is an input signal similar to the training sample $\boldsymbol{x}^m$, that is

$$\hat{\boldsymbol{x}}^m = \boldsymbol{x}^m + \boldsymbol{d} \tag{33}$$

where $\boldsymbol{d} = [d_1, \ldots, d_n]^T$ and d_i is a small random variable. Therefore, due to the interference of $\boldsymbol{d}$, the variation generated by the network output is as

$$\delta\hat{\boldsymbol{y}}^m = \boldsymbol{f}(\boldsymbol{x}^m + \boldsymbol{d}) - \boldsymbol{f}(\boldsymbol{x}^m) \approx (\partial \boldsymbol{f}(\boldsymbol{x}^m)/\partial \boldsymbol{x})\boldsymbol{d} \tag{34}$$

where $\partial \boldsymbol{f}(\boldsymbol{x}^m)/\partial \boldsymbol{x} = [\partial f_i/\partial x_i]$. Assuming $\boldsymbol{d}$ is a random vector independent of $\boldsymbol{x}^m$, and its mean and variance are as

$$\langle \boldsymbol{d} \rangle = \boldsymbol{O},\ \left\langle \boldsymbol{d}\boldsymbol{d}^T \right\rangle = \sigma^2 \boldsymbol{E}_n \tag{35}$$

where $\langle \cdot \rangle$ represents the mathematical expectation of the random variable, and $\boldsymbol{E}_n$ is the identity matrix of size n.

If the mean ratio of the variances of $|\delta\hat{\boldsymbol{y}}^m|$ and $|\boldsymbol{d}|$ is defined as the sensitivity S of the ANN, then

$$S = \sum_m \left\langle |\delta\hat{\boldsymbol{y}}^m|^2 \right\rangle \Big/ \left\langle |\boldsymbol{d}|^2 \right\rangle = \sum_m \left\langle \delta\hat{\boldsymbol{y}}^{(m)T} \delta\hat{\boldsymbol{y}}^{(m)} \right\rangle \Big/ \langle \boldsymbol{d}^T \boldsymbol{d} \rangle. \tag{36}$$

According to (29) and (30), S can be approximated as (the detailed calculation process is shown in the Appendix)

$$S \approx \sum_m \left\| \partial \boldsymbol{f}(\boldsymbol{x}^m)/\partial \boldsymbol{x} \right\|^2 / n \tag{37}$$

where $\| \cdot \|$ represents the Euclidean norm of a matrix, which is specifically defined as $\|\boldsymbol{A}\|^2 = \mathrm{tr}\ (\boldsymbol{A}\boldsymbol{A}^{\mathrm{T}}) = \sum_{i,j} \mathrm{a}_{ij}^2 (\boldsymbol{A} = [\mathrm{a}_{ij}])$.($\mathrm{tr}(\cdot)$ represents the trace of a matrix.)

Clearly, a smaller sensitivity S indicates that the ANN is less sensitive to new input data that is similar to the training data. Therefore, it would be logical to aim for the smallest possible values of both Q and S. This concept gives rise to the following

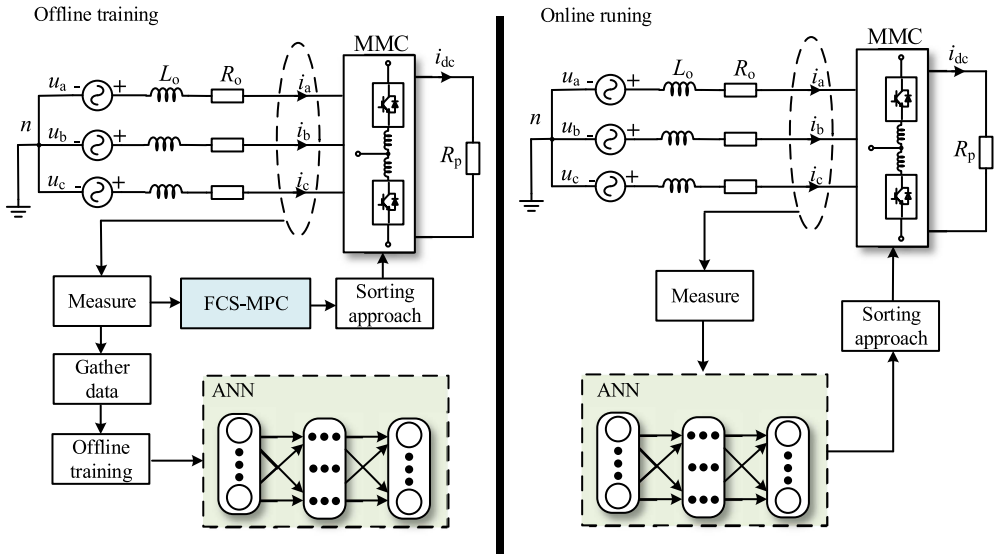

Fig. 10. Process of ANN emulating cascaded FCS-MPC.

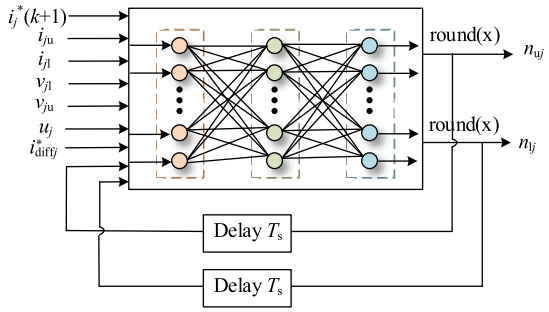

Fig. 11. ANN structure with a delay compensation strategy.

objective function that needs to be minimized:

$$R = Q + \alpha S = \sum_m \left\{ |\boldsymbol{y}^m - \boldsymbol{f}(\boldsymbol{x}^m)|^2 + (\alpha/n)\|\partial \boldsymbol{f}(\boldsymbol{x}^m)/\partial \boldsymbol{x}\|^2 \right\} \quad (38)$$

where α ($\alpha > 0$) is a weighting parameter.

Equation (38) indicates that minimizing R can both minimize the error function Q and reduce the sensitivity of ANN. In other words, minimizing (38) can enhance the generalization ability of ANN while updating its weights **W** and biases **B**. This can be achieved through the BP algorithm without any changes. Thus, a well-trained ANN can produce the correct output even for input data that has not been trained, as long as the input data does not deviate too much from the trained data. As a result, ANN exhibits strong robustness and adaptability, which allows it to maintain good control performance even under different grid impedances and nonideal grids.

It is worth mentioning that adding noise to the input data can enhance the generalization capability of ANN [36]. Therefore, in this paper, fluctuations are introduced in the grid voltage and the parameters of the MMC to improve the generalization capability of the ANN. The detail of adding noise is shown in Section IV-F.

TABLE I
PARAMETER FLUCTUATION RANGE

Parameters	Value
Grid-side voltage u_s	±7%
DC-bus voltage V_{dc}	±5%
Submodule capacitance C_{sm}	±10%
AC-side inductance L_o	±20%
Arm inductance L_i	±20%

F. Data Collection and Training Steps

In order to collect sufficient data for training ANN, an accurate MMC rectifier model using an overall control strategy is run in MATLAB/Simulink. The overall control strategy will be explained in detail in Section V. To make ANN suitable for various MMC rectifier operating conditions, ANN is trained at various power levels. Since the ac-side power in the simulation ranges from 0 to 6 MW, the equivalent resistance on the dc-side ranges from open circuit to 65 Ω. The dc-side resistance of MMC is determined by taking 35 resistance values, ranging from small to large and ultimately to open circuit, within the resistance range of 65 Ω to open circuit. The experiment uses the same methodology for gathering data as the simulation. Up to the open circuit, the dc-side resistance steadily rises from 30 Ω. The 35 sets of data allow the ANN to be configured to operate under a variety of power situations.

The grid voltage and parameters of MMC must fluctuate within a specified range in order to guarantee the resilience of ANN and its adaptation to the grid. Simulation and experiment follow the same parameter fluctuation rules. When the grid and parameters of MMC fluctuate within a certain range, the grid voltages, arm currents and arm voltages of MMC will change, which is equivalent to adding noise to the training data of ANN. This article presents fluctuations of grid voltage, dc-side voltage, submodule capacitance, ac-side inductance, and arm inductance, as shown in Table I. At 35 different power levels, the above-mentioned parameters are randomly selected within

TABLE II
TRAINING RESULTS

	Nodes of hidden layer	Data amount	Training time	Training accuracy	epoch
Simulation	6	6,300,000	0:01:09	96.0%	110
experiment					
ANN with delay compensation	4	7,700,000	0:05:02	89.7%	413
ANN without delay compensation	4	6,300,000	0:02:16	88.8%	440

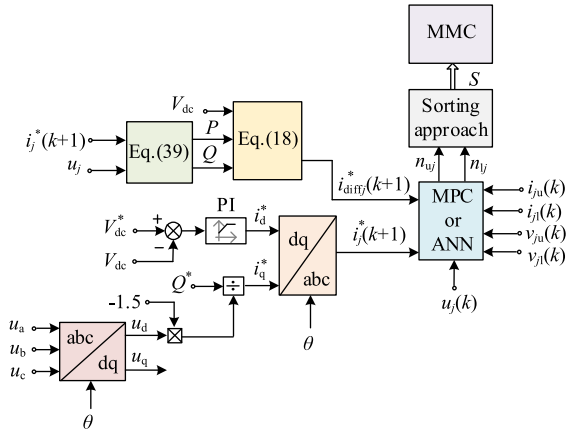

Fig. 12. Overall control strategy for MMC-based active rectifier.

the fluctuation range. A total of 20 000 data points are gathered for each input and output of cascaded FCS-MPC at each power level. Because there are seven inputs and two outputs, a total of 6 300 000 bits of data are collected for simulation and ANN without delay compensation (see Fig. 9). Because there are two outputs and nine inputs for the ANN with delay compensation (see Fig. 11), a total of 7 700 000 data are gathered.

After collecting data, use the "*trainlm*" function in MATLAB Deeping Learning Toolbox to train the ANN. The training results of the simulation and experiment are shown in Table II. The experiment is divided into ANN with delay compensation and ANN without delay compensation. Table II demonstrates that the simulation exhibits higher training accuracy as a result of the extensive nodes of hidden layers. Due to the larger amount of data in ANNs with delay compensation, more training time is required.

V. Overall Control Strategy for the MMC-Based Active Rectifier

Fig. 12 shows the overall dual control loop for an MMC-based active rectifier. Cascaded FCS-MPC or ANN is used as the inner current loop to output the inserted number of submodules in the upper arm and lower arm. To maintain the dc-bus voltage V_{dc} at the voltage reference value $V^*{}_{\mathrm{dc}}$, an outer dc-bus voltage control loop with a PI controller is used. The phase-locked loop is used to lock the grid-side voltage to obtain the grid angle θ. The output of the outer dc-bus voltage control loop through the PI controller is the active component of the grid-side current reference $i^*{}_{\mathrm{d}}$.

TABLE III
SIMULATION PARAMETERS

Parameters	Value
Rated power of the MMC S_{n}	6 MVA
Grid-side voltage u_{s}	10 kV
Submodule number per arm N	10
Grid-side inductance L_{o}	5 mH
DC-bus voltage V_{dc}	20 kV
Submodule capacitance C_{sm}	3300 μF
Arm inductance L_{i}	10 mH
DC-bus load resistance R_{p}	100 Ω
Sampling Period T_{s}	125 μs

According to instantaneous power theory

$$\begin{cases} P = u_{\mathrm{a}}i_{\mathrm{a}} + u_{\mathrm{b}}i_{\mathrm{b}} + u_{\mathrm{c}}i_{\mathrm{c}} \\ Q = \frac{1}{\sqrt{3}}[(u_{\mathrm{a}} - u_{\mathrm{b}})i_{\mathrm{c}} + (u_{\mathrm{b}} - u_{\mathrm{c}})i_{\mathrm{a}} + (u_{\mathrm{c}} - u_{\mathrm{a}})i_{\mathrm{b}}] \end{cases}. \quad (39)$$

When (36) is converted to the dq coordinate system, the expression of active power and reactive power is as follows:

$$\begin{cases} P = 1.5(u_{\mathrm{d}}i_{\mathrm{d}} + u_{\mathrm{q}}i_{\mathrm{q}}) \\ Q = 1.5(u_{\mathrm{q}}i_{\mathrm{d}} - u_{\mathrm{d}}i_{\mathrm{q}}) \end{cases}. \quad (40)$$

If the grid-side voltage is oriented to the d-axis, then $u_{\mathrm{q}} = 0$. Thus, (40) can be simplified as

$$\begin{cases} P = 1.5u_{\mathrm{d}}i_{\mathrm{d}} \\ Q = -1.5u_{\mathrm{d}}i_{\mathrm{d}} \end{cases}. \quad (41)$$

Therefore, the reactive component of the grid-side current reference $i^*{}_{\mathrm{q}}$ is $Q^*/(-1.5u_{\mathrm{d}})$. Q^* is the reactive power reference value. To ensure that the system power factor remains constant as 1, Q^* is set as 0 in this article. u_{d} is the d-axis component of the grid-side voltage. The active power P and reactive power Q of the system can be calculated in real time according to (39), and calculations of the circulating current reference value $i^*{}_{\mathrm{diff}j}(k+1)$ can be made in accordance with (18).

VI. Simulation and Experimental Results

A. Simulation Results

To validate the effectiveness of the ANN algorithm proposed in this article, a simulation of the MMC-based active rectifier is constructed in MATLAB/Simulink. The parameters of the simulation are shown in Table III.

Since the submodule capacitor stores energy and transports currents in the MMC, its design is essential. It is crucial to balance the capacitor size against the requirements for submodule voltage ripple. Generally, the submodule ripple voltage is kept below ±5% by selecting a cell capacitor. Based on a permitted peak-to-peak ripple magnitude for the submodule capacitor voltage, the capacitance value of the submodule can be computed [37]

$$C_{\mathrm{sm}} = \frac{S_{\mathrm{n}}}{3Nmu_{Cr}\Delta u_{\mathrm{c}}\omega\cos\varphi}\left[1 - \left(\frac{m\cos\varphi}{2}\right)^2\right]^{\frac{3}{2}} \quad (42)$$

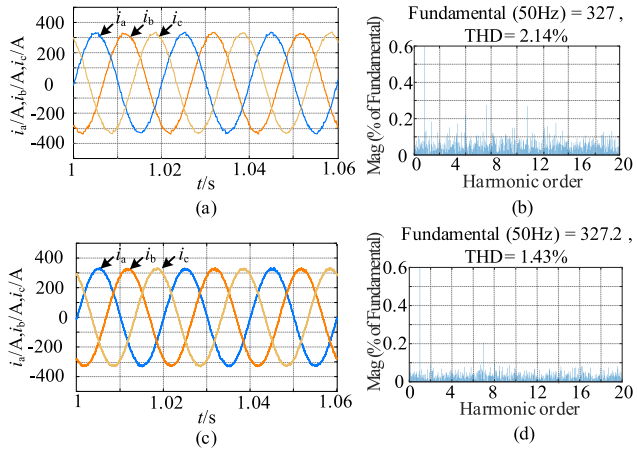

Fig. 13. Simulation results of external steady-state performance of cascaded FCS-MPC and ANN. (a) Three-phase grid-side current of cascaded FCS-MPC. (b) Phase-a grid-side current spectrum of cascaded FCS-MPC. (c) Three-phase grid-side current of ANN. (d) Phase-a grid-side current spectrum of ANN.

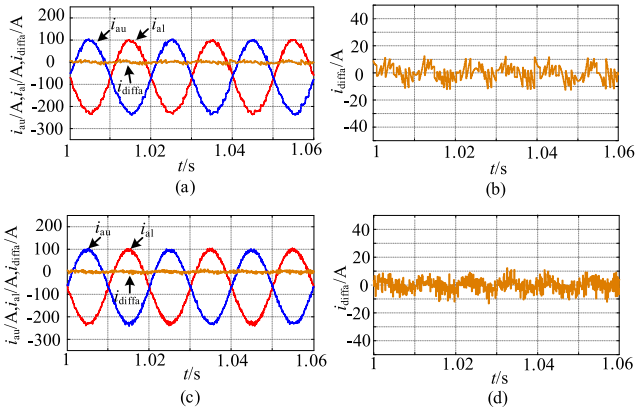

Fig. 14. Simulation results of the internal steady-state performance of cascaded FCS-MPC and ANN. (a) Upper arm current, lower arm currant, and circulating current of phase-a of cascaded FCS-MPC. (b) Enlarged view of the circulating current of phase-a of cascaded FCS-MPC. (c) Upper arm current, lower arm currant, and circulating current of phase-a of ANN. (d) Enlarged view of the circulating current of phase-a of ANN.

where m is the modulation index, u_{Cr} is the rated voltage of the submodule, Δu_c is the allowable fluctuation in the voltage of the submodule capacitor, and cosφ is the power factor angle. When MMC only transmits active power, power factor angle cos$\varphi = 1$. In the simulation, the modulation index m is 0.816. The maximum allowable fluctuation range of the submodule is $\pm 5\%$, then $\Delta u_c = 5\% Uc = 100$ V. Therefore, C_{sm} can be calculated as 2970 μF. Considering a certain margin, take 3300 μF capacitor as the final submodule capacitance value.

Similarly, the selection of arm inductance is also significant. If the arm inductance is too small, it will cause a large circulating current and more harmonic currents in the MMC rectifier. If the arm inductance is too large, it will affect the current tracking speed of the control system, increase the system volume, and increase the cost. Therefore, it is necessary to reasonably select the size of the arm inductance. In order to meet the requirements of circulating current second harmonic, maximum arm ripple current, resonance with the submodule capacitance, and the short-circuit current limit, based on the worst voltage jump of the arm during the transient process, an approximate calculation formula for the arm inductance is obtained [38]

$$L_i = \frac{U_{c\max}}{4m\Delta i_{arm\max} f_s} \tag{43}$$

where U_{cmax} is the maximum voltage of the submodule capacitor. Δi_{armmax} is the maximum ripple value of the arm current. f_s is the switching frequency of MMC.

The maximum allowable ripple of the arm is set to 20%. The value of f_s is taken as 1500 Hz in this article. As a result, the arm inductance L_i can be calculated to be 7.8 mH. Considering a certain margin, take $L_i = 10$ mH.

The external steady-state three-phase grid-side current of a cascaded FCS-MPC and ANN is shown in Fig. 13(a) and (c). Their spectrum is shown in Fig. 13(b) and (d). Both of the two methods, as can be seen, are able to attain excellent steady-state performance and low THD characteristics. The THD of cascaded FCS-MPC is 2.14%, as shown in the figures, but the THD of ANN is 1.43%, demonstrating that ANN achieves greater steady-state performance.

Fig. 14(a) shows upper arm current, lower arm currant, and circulating current of phase-a of cascaded FCS-MPC. Fig. 14(b) is the enlarged view of the circulating current in Fig. 14(a). As indicated in Fig. 14(b), the second stage control successfully suppresses the circulation current, which has an amplitude of -10 to 10 A. The phase-a upper arm, lower arm, and circulating currents of the ANN are shown in Fig. 14(c), and the larger version of the circulating current is shown in Fig. 14(d). As compared to cascaded FCS-MPC, the control impact of ANN on arm currents and circulating currents is nearly identical. The circulating current is likewise successfully suppressed, and the arm currents of phase-a exhibit comparable quasi-sinusoidal characteristics.

In order to verify the dynamic response of ANN, the load on the dc-bus is set to change from 120 to 100 Ω at 2.5 s. As shown in Fig. 15(a), when the dc-bus load abruptly changes, the active power reference P^* immediately shifts from 3.3 to 4 MW. It is clear that the actual active power P rapidly follows the reference value P^* and eventually remains at 4 MW. The voltage of dc-bus V_{dc} is shown in Fig. 15(b) when there is an abrupt change in the dc-bus load. The diagram demonstrates how, in the event of a load disturbance, the actual value of the dc-bus voltage V_{dc} fluctuates briefly before quickly returning to the reference value V^*_{dc}. When the dc-bus load changes abruptly, the three-phase grid-side currents are depicted in Fig. 15(c). Similarly, during the dc-bus load fluctuation, the grid-side currents can be quickly updated. Fig. 15(d) shows the first submodule capacitor voltage on the a-phase upper and lower arms during a dc side load mutation. The figure shows how, before the dc-bus load mutation, the submodule capacitor voltage fluctuates around 2000 V and quickly stabilizes at roughly 2000 V after the dc-bus load mutation. The voltage fluctuation of the submodule capacitors grows as active power transmission increases. Consequently, Fig. 15 demonstrates that the ANN has good dynamic performance.

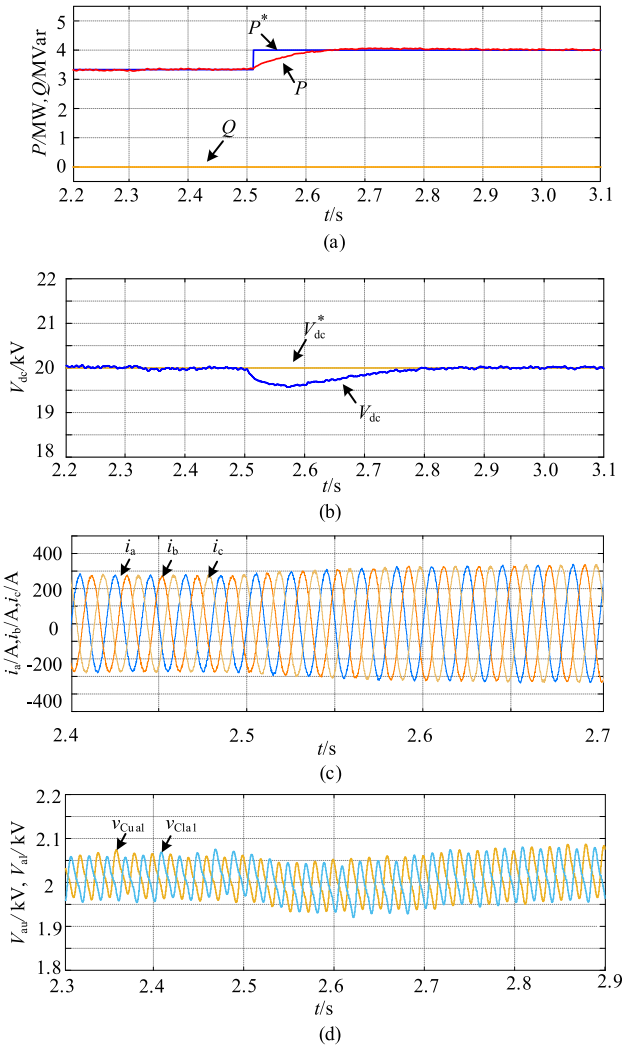

Fig. 15. Simulation results of transient-state performance of ANN. (a) Active power and reactive power. (b) DC-bus voltage. (c) Three-phase grid-side currents. (d) Capacitor voltages of the first submodule in the upper arm and lower arm of phase-a.

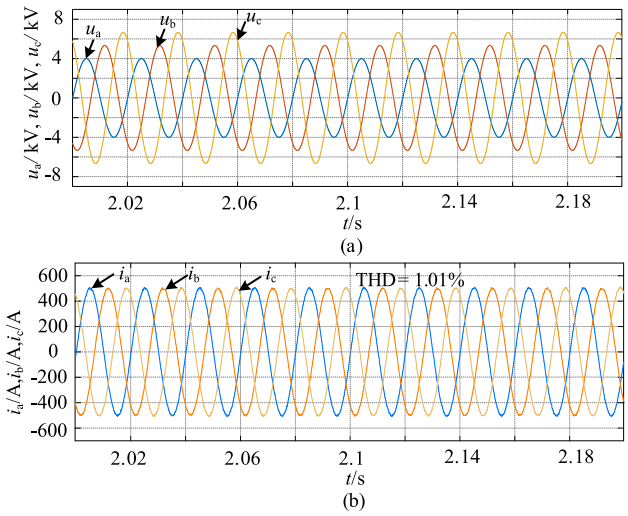

Fig. 16. Simulation results of ANN under unbalanced grid voltage condition. (a) Grid-side voltage. (b) Grid-side current.

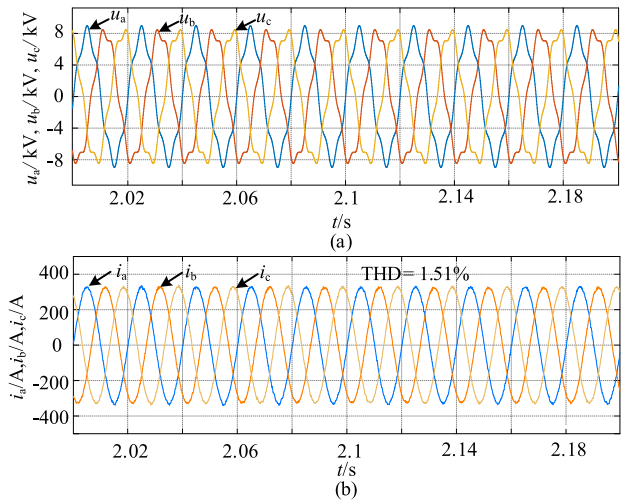

Fig. 17. Simulation results of ANN under distorted grid voltage condition. (a) Grid-side voltage. (b) Grid-side current.

To verify the adaptability of ANN under unbalanced grid voltage conditions, Fig. 16 shows the grid-side voltage and grid-side current of ANN under unbalanced grid voltage conditions, where the three-phase voltage is set to 60%, 80%, and 100% of the nominal value, respectively. When the grid-side voltage is lower than the normal value, the positive-sequence voltage will decrease. As the outer loop in this article adopts a constant dc-bus voltage control mode, the grid-side current will increase to ensure the transfer of power of dc-bus, as shown in Fig. 16(b). As can be seen, although the grid voltage is severely unbalanced, the grid-side current remains balanced with a THD of only 1.01%, which is completely unaffected by the unbalance on the grid side. This demonstrates the generalization and fault tolerance of ANN. Even if an unbalanced grid leads to biased input data for ANN, it can still produce accurate outputs, thus enhancing the adaptability of the power grid.

To verify the adaptability of ANN under distorted grid voltage conditions, 10% of the 5th harmonic is introduced into the grid, as shown in Fig. 17(a). Fig. 17(b) shows the grid-side current when ANN is adopted. It can be seen that even though the grid is severely distorted, the grid current remains a three-phase sine wave with a THD of 1.51%, indicating that it is not affected by the distorted grid. Similarly, in the case of a distorted grid, the distortion of the power grid leads to a bias in the input training data of ANN that is based on the ideal power grid. However, owing to the nonlinear filtering characteristics and generalization of ANN, the output of ANN remains accurate. Therefore, the simulation results demonstrate that ANN has good adaptability to grid distortion.

Simulations are run on both methods under parameter mismatch situations to confirm that ANN had superior adaptability and robustness over cascaded FCS-MPC. The mismatch varies between 4 and 6 mH for the grid-side inductance and between 8 and 12 mH for the arm inductance. The grid-side current's THD under parameter mismatch is shown in Fig. 18. It can be shown that cascaded FCS-MPC has a greater THD and

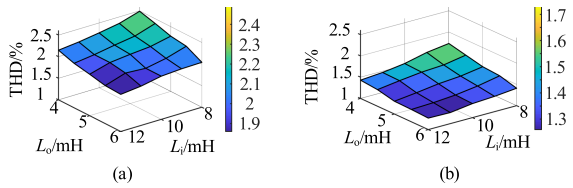

Fig. 18. Simulation results of cascaded FCS-MPC and ANN when gird and MMC parameters are mismatched. (a) Grid-side current THD of cascaded FCS-MPC. (b) Grid-side current THD of ANN.

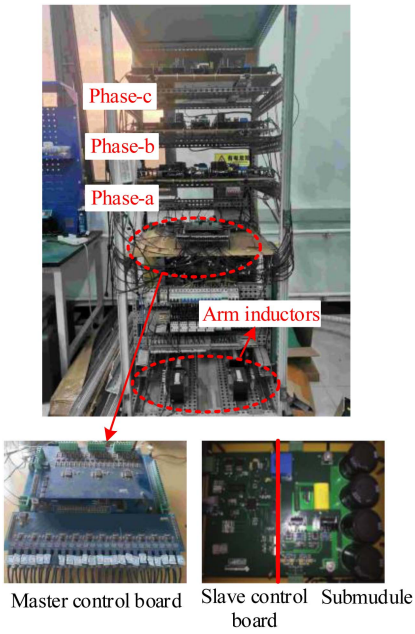

Fig. 19. MMC-based active rectifier experimental prototype.

is more susceptible to parameter mismatch. On the contrary, ANN displays lower THD in grid-side current under parameter mismatch due to its stronger tolerance to parameters. This is because cascaded FCS-MPC relies on mathematical models for control. When there are changes in the actual model or grid, it deviates from the original FCS-MPC model and negatively affects the output of cascaded FCS-MPC. In contrast, ANN is based on data learning and does not rely on specific mathematical models. It has strong generalization and fault tolerance. Even when there are changes in the actual model or grid, ANN can still provide correct outputs. As a result, ANN demonstrates stronger adaptability to grid impedance and better robustness.

E. Experimental Results

To verify the effectiveness of the algorithm proposed in this article, a downscaled five-level MMC-based active rectifier experimental prototype was built as shown in Fig. 19. The entire control system is constructed by a two-layer structure. The master control board, which consists of a DSP (TI-TMS320F28335) and an FPGA (Xilinx-XC3S500E), is the top layer structure. The three ADCs (ADI-AD7656) are used to sample grid-side voltages, currents, and arm currents. The DSP is mainly used for executing the outer dc-bus loop and the calculation of ANN or MPC, and the FPGA mainly executes the sorting algorithm.

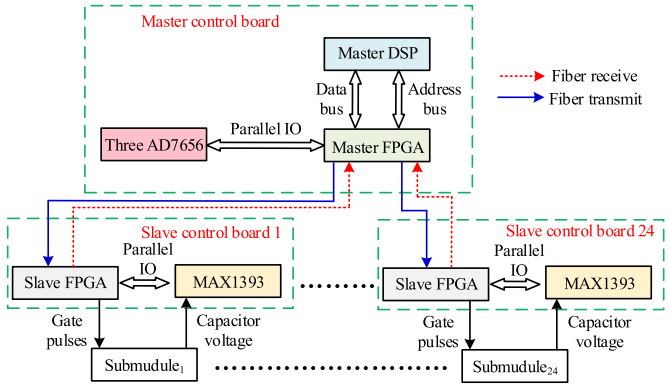

Fig. 20. Entire two-layer control system.

TABLE IV
EXPERIMENTAL PARAMETERS

Parameters	Value
Grid-side voltage u_s	100 V
Submodule number per arm N	4
Grid-side inductance L_o	15 mH
DC-bus voltage V_{dc}	200 V
Submodule capacitance C_{sm}	1880 μF
Arm inductance L_i	4 mH
DC-bus load resistance R_p	100 Ω
Sampling period T_s	125 μs

The second layer structure contains 24 slave control boards. Each slave control board has an FPGA (Xilinx-XC3S200A) and an ADC (MAXIM-MAX1393) to sample 24 submodule capacitor voltage. Optical fibers link the master control board to the slave control board. Switching combinations are sent from the master control board to the slave control board. By the sorting approach and pulse signals processing, the final gate pulses are generated. Meanwhile, the master control board receives 24 submodule capacitor voltages from the slave control board. Universal asynchronous receiver/transmitter protocol is used as the method of communication between the two control boards. The entire two-layer control system is shown in Fig. 20.

The experimental parameters are shown in Table IV. Similar to simulation, 35 sets of data were collected in the experiment under a variety of working conditions, namely, the dc-bus load varies from no load to full load. Also, the range of parameter fluctuations remains consistent with Table II.

In Fig. 21, the steady-state grid-side voltage, current, and dc-side voltage of phase-a for cascaded FCS-MPC and ANN are shown. The grid-side current of phase-a for both methods is sinusoidal, and the dc-bus voltage is stabilized at its reference value, as can be seen in Fig. 21(a) and (c). It is clear from Fig. 21(b) and (d) that both algorithms maintain the excellent grid-side current harmonic properties. Because the THD of ANN is 1.4% and that of cascaded FCS-MPC is 2.1%, ANN clearly shows better harmonic characteristics.

The upper arm current, lower arm current, and circulating current of phase-a for cascaded FCS-MPC and ANN are shown in Fig. 22. Similar to the simulation, it can be observed that under

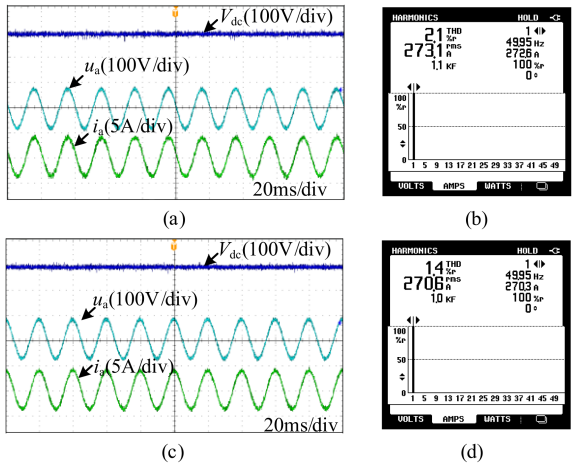

Fig. 21. Experimental results of the external steady-state performance of cascaded FCS-MPC and ANN. (a) Phase-a grid-side voltage, current, and DC-bus voltage of cascaded FCS-MPC. (b) Phase-a grid-side current power quality analysis results of cascaded FCS-MPC. (c) Phase-a grid-side voltage, current, and DC-bus voltage of ANN. (d) Phase-a grid-side current power quality analysis results of ANN.

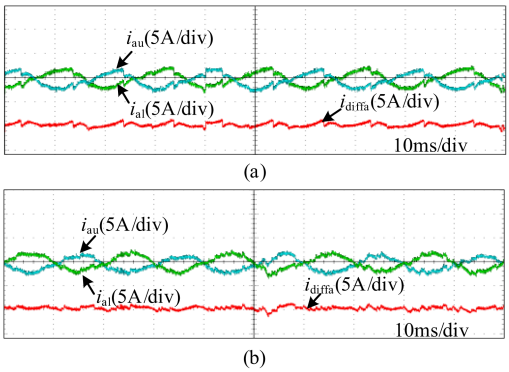

Fig. 22. Experimental results of internal steady-state performance of cascaded FCS-MPC and ANN. (a) Upper arm current, lower arm currant, and circulating current of phase-a of cascaded FCS-MPC. (b) Upper arm current, lower arm currant, and circulating current of phase-a of ANN.

both algorithms, the arm currents exhibit quasi-sinusoidal characteristics, and the circulating current is effectively suppressed.

The dc-bus voltage, phase-a grid side voltage, and current are shown in Fig. 23(a) when the dc-bus load is abruptly reduced from 200 to 100 Ω. After a brief oscillation, it can be seen that the dc-bus voltage soon returns to the reference value of 200 V, the grid side voltage stays constant, and the grid side current slightly increases and reaches the corresponding value quickly. When the load is suddenly changed, the first submodule capacitor voltage on the phase-a upper and lower arms is shown in Fig. 23(b). The voltage of the submodule capacitor returns to about 50 V after a brief adjustment when the dc-bus load is abruptly adjusted. As a result, it can be concluded that ANN performs a great transient state.

Fig. 24 presents a comparison of experimental results under unbalanced grid conditions for cascaded FCS-MPC and ANN. Fig. 24(a) shows the unbalanced grid voltage, which is consistent with the simulation. Here, the voltage values of phase a, b, and c are respectively set to 60%, 80%, and 100% of the normal

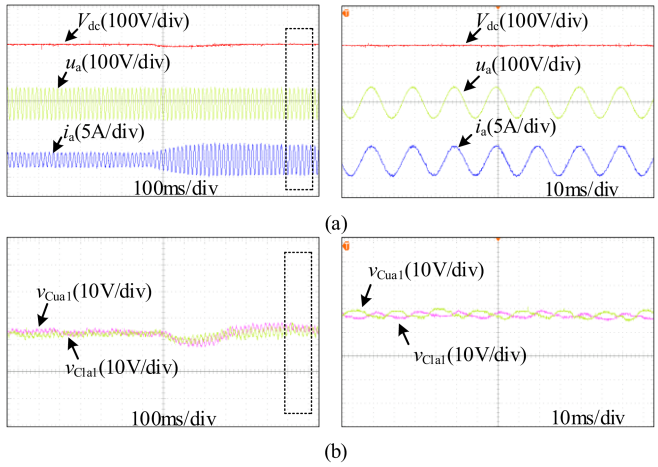

Fig. 23. Experimental results of the transient-state performance of ANN. (a) Phase-a grid-side voltage, current, and DC-bus voltage of ANN. (b) Capacitor voltages of the first submodule in the upper arm and lower arm of phase-a.

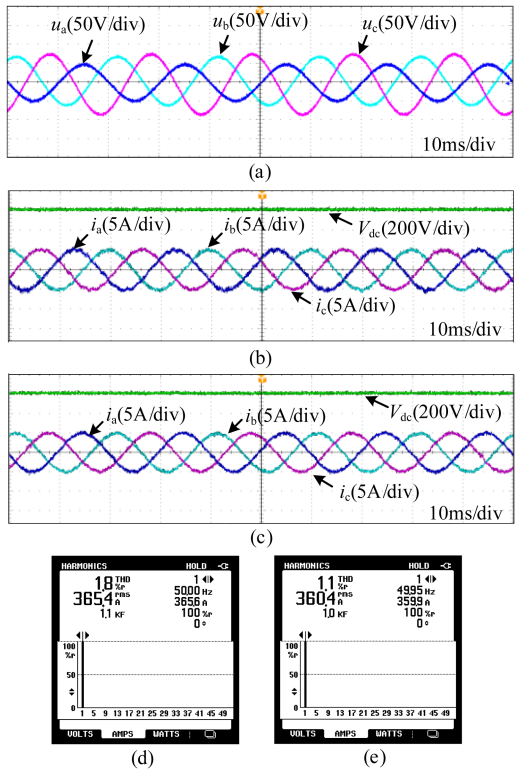

Fig. 24. Experimental comparison between cascaded FCS-MPC and ANN under unbalanced grid voltage condition. (a) Three-phase unbalanced grid-side voltage. (b) Three-phase grid-side current of cascaded FCS-MPC. (c) Three-phase grid-side current of ANN. (d) Phase-a grid-side current power quality analysis results of cascaded FCS-MPC. (e) Phase-a grid-side current power quality analysis results of ANN.

voltage value. It can be observed from Fig. 24(b) and (c) that grid-side currents of both cascaded FCS-MPC and ANN exhibit good performance under unbalanced grid conditions. However, from Fig. 24(d) and (e), it can be seen that the THD of grid-side currents of ANN is still much smaller than that of cascaded FCS-MPC. Similar to simulations, in an unbalanced grid scenario, the input data of ANN may deviate from the input data based on the

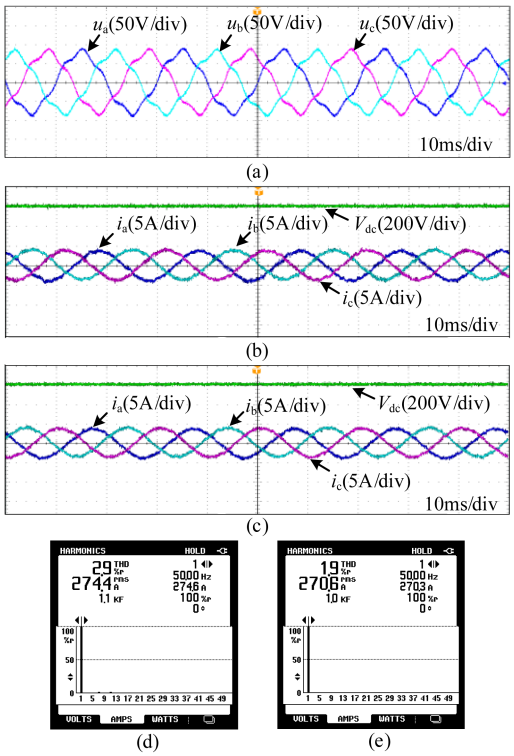

Fig. 25. Experimental comparison between cascaded FCS-MPC and ANN under distorted grid voltage condition. (a) Three-phase distorted grid-side voltage. (b) Three-phase grid-side current of cascaded FCS-MPC. (c) Three-phase grid-side current of ANN. (d) Phase-a grid-side current power quality analysis results of cascaded FCS-MPC. (e) Phase-a grid-side current power quality analysis results of ANN.

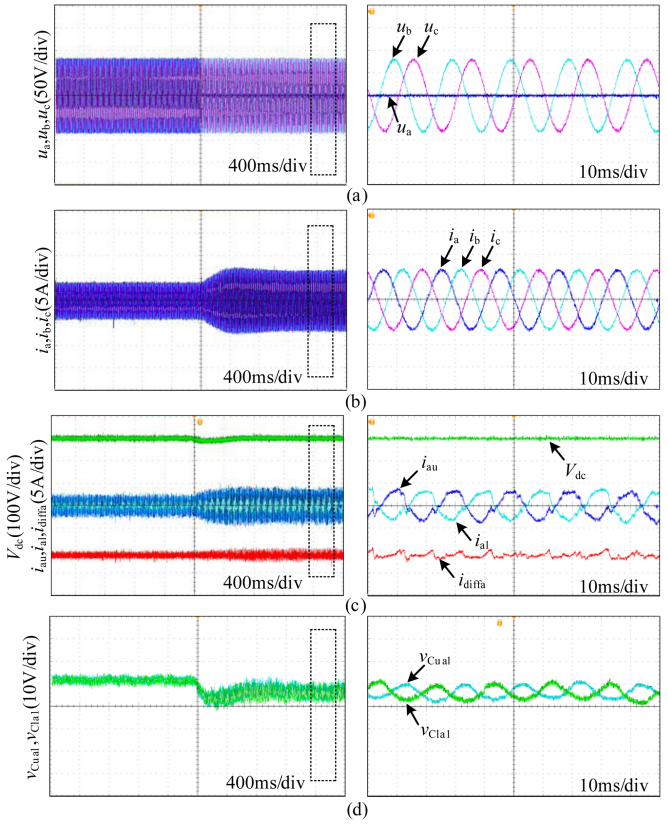

Fig. 26. Experimental results of ANN under single-phase-to-ground fault. (a) Three-phase grid-side voltage. (b) Three-phase grid-side current (c) Upper arm current, lower arm current, circulating current of phase-a and DC-bus voltage. (d) Capacitor voltages of the first submodule in the upper arm and lower arm of phase-a.

ideal grid. However, due to the generalization and fault-tolerance of ANN, it can still generate correct outputs. Consequently, ANN demonstrates excellent adaptability and superior performance under unbalanced grid conditions even if the training data for ANN is an ideal grid.

Fig. 25 presents the experimental results of cascaded FCS-MPC and ANN under distorted grid conditions. Fig. 25(a) shows the distorted grid, which is consistent with the simulation. Here, 10% of 5th harmonic is injected into the ideal grid. Fig. 25(b) and (c) shows the three-phase grid-side currents of cascaded FCS-MPC and ANN under distorted grid conditions, respectively. As can be seen, cascaded FCS-MPC and ANN can achieve good grid-side currents even under distorted grid conditions. Nevertheless, in Fig. 25(d) and (e), it can be seen that the THD of the grid-side current of ANN is still smaller than that of cascaded FCS-MPC. Likewise, a distorted grid results in input data deviation for ANN. However, the fault tolerance and generalization of ANN enable it to still generate correct outputs. As a consequence, ANN shows better grid adaptability and performance under the distorted grid even if the training data for ANN is an ideal grid.

To further demonstrate the adaptability of ANN to the grid, Fig. 26 shows the experimental results of ANN under single-phase-to-ground fault. Fig. 26(a) shows the ac-side voltages. When the single-phase-to-ground fault occurs, the voltage of phase-a suddenly changes to 0, while phase-b and phase-c remain unchanged. In Fig. 26(b), it can be seen that when the single-phase-to-ground fault occurs, the ac-side currents rapidly increase to maintain stable power transmission. As demonstrated in Fig. 26(c), the arm currents rapidly increase in a manner similar to the ac-side currents. At the same time, the circulating currents also increase correspondingly. This is because the circulating currents have both negative-sequence and zero-sequence components. Fig. 26(d) shows the voltage of the submodule capacitor. Because of the presence of negative-sequence and zero-sequence voltage in the dc-side voltage, its fluctuation value also increases. Consequently, despite the fact that ANN is only trained in ideal grid scenarios, its fault tolerance and generalization allow it to function correctly even in the event of the single-phase-to-ground fault, indicating its excellent grid adaptability.

In order to verify that ANN has better grid adaptability and robustness than cascaded FCS-MPC, the harmonic characteristics of the two algorithms are compared under the condition that the grid-side inductance changes from 10, 15 to 20 mH, and the arm inductance varies between 3, 4, and 5 mH. Fig. 27 shows the grid-side current THD of the two algorithms when inductance parameters are mismatched. As can be shown, with cascaded FCS-MPC control, the grid-side current THD is significantly high in the case of parameter mismatches. The grid-side current THD is still low under ANN control in the case of parameter

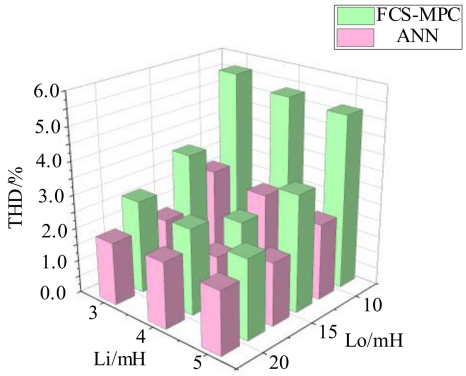

Fig. 27. Experimental results of cascaded FCS-MPC and ANN when grid and MMC parameters are mismatched.

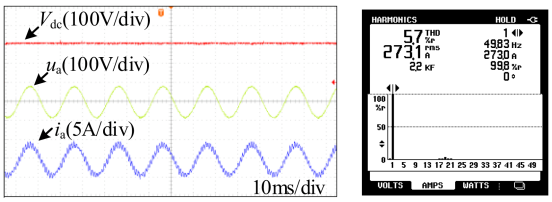

(a) (b)

Fig. 28. ANN without delay compensation. (a) Phase-a grid-side voltage, current, and DC-bus voltage. (b) Power quality analysis results.

mismatches, and it is lower than that of cascaded FCS-MPC in all parameter mismatch scenarios. Similar to simulations, this is because of the inherent drawback of FCS-MPC, which relies on mathematical models for control. When the actual model or grid parameters change for various reasons, the FCS-MPC model may no longer be adapted to the altered model, leading to control deterioration. However, the fault tolerance and generalization of ANN can avoid this drawback. When grid parameters or the actual model deviates, ANN can not only filter out input noise caused by the deviation but also adapt to the change in power grid parameters or changed model, exhibiting good power grid adaptability and robustness. As a result, ANN shows much better grid adaptability and robustness than cascaded FCS-MPC.

Fig. 28 shows the grid-side voltage, current, and dc-bus voltage of phase-a without delay compensation. As can be observed, ANN can also achieve steady dc-bus voltage without delay compensation, and the grid-side current is sinusoidal. However, because of the inherent computational delay of the digital controller, the grid-side current contains unnecessary ripple, leading to a large increase in THD and deterioration of control performance. Compared with Fig. 21(c) and (d), the ANN with delay compensation technique significantly lowers the ripple of the grid-side current, resulting in a sharp reduction in THD. Therefore, the proposed delay compensation strategy for ANN in this article solves the problem of deterioration of ANN control performance caused by computational delay.

To evaluate the calculation burden under cascaded FCS-MPC and ANN, the overall program execution time of these two methods in one sampling period is shown in Fig. 29. The signal

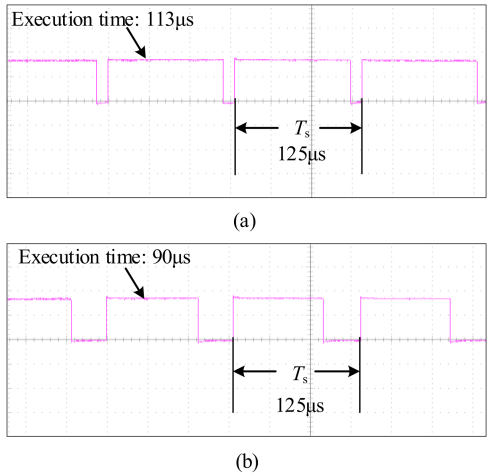

Fig. 29. Overall execution time of the two methods. (a) Cascaded FCS-MPC. (b) ANN.

is set to one and zero at the start and the end of these two approaches, respectively. As can be seen from the comparison, the overall execution time of cascaded FCS-MPC is around 113 μs, while the overall execution time of ANN is about 90 μs, which indicates that ANN's computational burden is lower than cascaded FCS-MPC. Furthermore, it should be emphasized that cascaded FCS-MPC's calculation burden increases dramatically with the rise of submodule numbers, while the calculation burden of ANN does not increase with the rise of submodule numbers. Therefore, ANN-based control strategies are suited for engineering applications.

VII. Conclusion

In this article, the grid adaptability of the MMC-based rectifier with the MPC implemented by the ANN technique is investigated. The data of cascaded FCS-MPC under ideal grid is used to train the ANN offline. Once trained, the ANN is used online to replace the cascaded FCS-MPC under nonideal grid, ideal grid, and varied grid impedance. Benefiting from the fault tolerance of ANN, it can function as a nonlinear filter to filter out noise in input data. At the same time, the generalization of ANN guarantees that it can produce accurate results as long as input fluctuations are within a certain range. These two aspects complement each other, providing the MMC-based rectifier controlled by the ANN with excellent grid adaptability and robustness. Simulations and experiments are implemented under an ideal grid, unbalanced grid, distorted grid, and varying grid impedance to validate the control accuracy, robustness, and grid adaptability of the ANN, with the results compared to cascaded FCS-MPC. It can be seen that the grid adaptability of the MMC-based rectifier is enhanced by employing ANN as the primary control algorithm. Besides, the proposed delay compensation strategy for ANN successfully ensures the control performance under the calculational delay of the digital controller. In conclusion, the studied MPC strategy implemented by the ANN technique could be an effective control manner for the MMCs connected to the nonideal grids.

APPENDIX

According to (29) and (30), (32) can be approximated as

$$
\begin{aligned}
S &= \sum_m \left\langle \delta\hat{\boldsymbol{y}}^{(m)T}\delta\hat{\boldsymbol{y}}^{(m)} \right\rangle / \left\langle \boldsymbol{d}^T\boldsymbol{d} \right\rangle \\
&\approx \sum_m \left\langle \boldsymbol{d}^T(\partial \boldsymbol{f}(\boldsymbol{x}^m)/\partial \boldsymbol{x})^T(\partial \boldsymbol{f}(\boldsymbol{x}^m)/\partial \boldsymbol{x})\boldsymbol{d} \right\rangle / \left\langle \boldsymbol{d}^T\boldsymbol{d} \right\rangle \\
&= \sum_m \left\langle \mathrm{tr}[(\partial \boldsymbol{f}(\boldsymbol{x}^m)/\partial \boldsymbol{x})\boldsymbol{d}\boldsymbol{d}^T(\partial \boldsymbol{f}(\boldsymbol{x}^m)/\partial \boldsymbol{x})^T] \right\rangle / \left\langle \mathrm{tr}(\boldsymbol{d}\boldsymbol{d}^T) \right\rangle \\
&= \sum_m \sigma^2 \mathrm{tr}\{[(\partial \boldsymbol{f}(\boldsymbol{x}^m)/\partial \boldsymbol{x}][\partial \boldsymbol{f}(\boldsymbol{x}^m)/\partial \boldsymbol{x}]^T\}/(n\sigma^2) \\
&= \sum_m \left\| \partial \boldsymbol{f}(\boldsymbol{x}^m)/\partial \boldsymbol{x} \right\|^2 / n.
\end{aligned}
$$

REFERENCES

[1] M. A. Perez, S. Bernet, J. Rodriguez, S. Kouro, and R. Lizana, "Circuit topologies, modeling, control schemes, and applications of modular multilevel converters," *IEEE Trans. Power Electron.*, vol. 30, no. 1, pp. 4–17, Jan. 2015.

[2] A. Dekka, B. Wu, R. L. Fuentes, M. Perez, and N. R. Zargari, "Evolution of topologies, modeling, control schemes, and applications of modular multilevel converters," *IEEE J. Emerg. Sel. Top. Power Electron.*, vol. 5, no. 4, pp. 1631–1656, Dec. 2017.

[3] H. Lin, C. Lin, D. Xie, P. Acuna, and W. Liu, "A counter-based open-circuit switch fault diagnostic method for a single-phase cascaded H-bridge multilevel converter," *IEEE Trans. Power Electron.*, vol. 39, no. 1, pp. 814–825, Jan. 2024.

[4] Z. Gong, X. Wu, P. Dai, and R. Zhu, "Modulated model predictive control for MMC-based active front-end rectifiers under unbalanced grid conditions," *IEEE Trans. Ind. Electron.*, vol. 66, no. 3, pp. 2398–2409, Mar. 2019.

[5] X. He, J. Peng, P. Han, Z. Liu, S. Gao, and P. Wang, "A novel advanced traction power supply system based on modular multilevel converter," *IEEE Access*, vol. 7, pp. 165018–165028, Oct. 2019.

[6] R. Li and L. Xu, "A unidirectional hybrid HVDC transmission system based on diode rectifier and full-bridge MMC," *IEEE J. Emerg. Sel. Top. Power Electron.*, vol. 9, no. 6, pp. 6974–6984, Dec. 2021.

[7] M. Hagiwara and H. Akagi, "Control and experiment of pulsewidth-modulated modular multilevel converters," *IEEE Trans. Power Electron.*, vol. 24, no. 7, pp. 1737–1746, Jul. 2009.

[8] Q. Tu, Z. Xu, and L. Xu, "Reduced switching-frequency modulation and circulating current suppression for modular multilevel converters," *IEEE Trans. Power Del.*, vol. 26, no. 3, pp. 2009–2017, Jul. 2011.

[9] J. Pou, S. Ceballos, G. Konstantinou, V. G. Agelidis, R. Picas, and J. Zaragoza, "Circulating current injection methods based on instantaneous information for the modular multilevel converter," *IEEE Trans. Ind. Electron.*, vol. 62, no. 2, pp. 777–788, Feb. 2015.

[10] A. Dekka, B. Wu, V. Yaramasu, R. L. Fuentes, and N. R. Zargari, "Model predictive control of high-power modular multilevel converters—An overview," *IEEE J. Emerg. Sel. Top. Power Electron.*, vol. 7, no. 1, pp. 168–183, Mar. 2019.

[11] B. Gutierrez and S. Kwak, "Modular multilevel converters (MMCs) controlled by model predictive control with reduced calculation burden," *IEEE Trans. Power Electron.*, vol. 33, no. 11, pp. 9176–9187, Nov. 2018.

[12] X. Chen, J. Liu, S. Song, S. Ouyang, H. Wu, and Y. Yang, "Modified increased-level model predictive control methods with reduced computation load for modular multilevel converter," *IEEE Trans. Power Electron.*, vol. 34, no. 8, pp. 7310–7325, Aug. 2019.

[13] J.-W. Moon, J.-S. Gwon, J.-W. Park, D.-W. Kang, and J.-M. Kim, "Model predictive control with a reduced number of considered states in a modular multilevel converter for HVDC system," *IEEE Trans. Power Del.*, vol. 30, no. 2, pp. 608–617, Apr. 2015.

[14] J. Huang et al., "Priority sorting approach for modular multilevel converter based on simplified model predictive control," *IEEE Trans. Ind. Electron.*, vol. 65, no. 6, pp. 4819–4830, Jun. 2018.

[15] Y. Sun, Z. Li, Y. Zhang, Y. Li, and Z. Zhang, "A time-domain virtual-flux based predictive control of modular multilevel converters for offshore wind energy integration," *IEEE Trans. Energy Convers.*, vol. 37, no. 3, pp. 1803–1814, Sep. 2022.

[16] W. Zhang, J. Zhang, Q. Wang, Y. Jiang, and G. Tan, "Dual-vector model predictive control for modular multilevel converter with low calculation burden," *IEEE Access*, vol. 12, pp. 28520–28530, Feb. 2024.

[17] P. Tuo, Z. Gong, X. Zheng, C. Zhao, and X. Wu, "Three-stage model predictive control for modular multilevel converters with comprehensive performance optimization," *J. Power Electron.*, to be published, doi: 10.1007/s43236-024-00789-2.

[18] V. R. Chowdhury and J. W. Kimball, "Control of a three-phase grid-connected inverter under non-ideal grid conditions with online parameter update," *IEEE Trans. Energy Convers.*, vol. 34, no. 3, pp. 1613–1622, Sep. 2019.

[19] M. M. Mardani, R. D. Lazar, N. Mijatovic, and T. Dragičević, "Artificial neural network-based constrained predictive real-time parameter adaptation controller for grid-tied VSCs," *IEEE J. Emerg. Sel. Top. Power Electron.*, vol. 11, no. 2, pp. 1507–1517, Apr. 2023.

[20] M. Zhang, Y. Zhang, and Q. Xu, "Transfer learning based online impedance identification for modular multilevel converters," *IEEE Trans. Power Electron.*, vol. 38, no. 10, pp. 12207–12218, Oct. 2023.

[21] S. Zhao, F. Blaabjerg, and H. Wang, "An overview of artificial intelligence applications for power electronics," *IEEE Trans. Power Electron.*, vol. 36, no. 4, pp. 4633–4658, Apr. 2021.

[22] D. Wang et al., "Model predictive control using artificial neural network for power converters," *IEEE Trans. Ind. Electron.*, vol. 69, no. 4, pp. 3689–3699, Apr. 2022.

[23] S. Wang, T. Dragicevic, G. F. Gontijo, S. K. Chaudhary, and R. Teodorescu, "Machine learning emulation of model predictive control for modular multilevel converters," *IEEE Trans. Ind. Electron.*, vol. 68, no. 11, pp. 11628–11634, Nov. 2021.

[24] M. Novak and T. Dragicevic, "Supervised imitation learning of finite set model predictive control systems for power electronics," *IEEE Trans. Ind. Electron*, vol. 68, no. 2, pp. 1717–1723, Feb. 2021.

[25] A. Bakeer, I. S. Mohamed, P. B. Malidarreh, I. Hattabi, and L. Liu, "An artificial neural network-based model predictive control for three-phase flying capacitor multilevel inverter," *IEEE Access*, vol. 10, pp. 70305–70316, Jul. 2022.

[26] T. Dragicevic and M. Novak, "Weighting factor design in model predictive control of power electronic converters: An artificial neural network approach," *IEEE Trans. Ind. Electron.*, vol. 66, no. 11, pp. 8870–8880, Nov. 2019.

[27] Q. Xu, T. Dragicevic, L. Xie, and F. Blaabjerg, "Artificial intelligence-based control design for reliable virtual synchronous generators," *IEEE Trans. Power Electron.*, vol. 36, no. 8, pp. 9453–9464, Aug. 2021.

[28] Y. Gao et al., "Inverse application of artificial intelligence for the control of power converters," *IEEE Trans. Power Electron.*, vol. 38, no. 2, pp. 1535–1548, Feb. 2023.

[29] S. Wang, T. Dragicevic, Y. Gao, S. K. Chaudhary, and R. Teodorescu, "Machine learning based operating region extension of modular multilevel converters under unbalanced grid faults," *IEEE Trans. Ind. Electron*, vol. 68, no. 5, pp. 4554–4560, May 2021.

[30] M. Guan and Z. Xu, "Modeling and control of a modular multilevel converter-based HVDC system under unbalanced grid conditions," *IEEE Trans. Power Electron.*, vol. 27, no. 12, pp. 4858–4867, Dec. 2012.

[31] S. Li, X. Wang, Z. Yao, T. Li, and Z. Peng, "Circulating current suppressing strategy for MMC-HVDC based on nonideal proportional resonant controllers under unbalanced grid conditions," *IEEE Trans. Power Electron.*, vol. 30, no. 1, pp. 387–397, Jan. 2015.

[32] P. Cortes, J. Rodriguez, C. Silva, and A. Flores, "Delay compensation in model predictive current control of a three-phase inverter," *IEEE Trans. Ind. Electron.*, vol. 59, no. 2, pp. 1323–1325, Feb. 2012.

[33] S. Haykin, *Neural Networks and Learning Machines*. Upper Saddle River, NJ, USA: Prentice Hall, 2008.

[34] D.E. Rumelhart, G. E. Hinton, and R.J. Williams, "Learning internal representations by error propagation," in *Parallel Distributed Processing*, D. E. Rumelhart and J. L. McClelland, Eds. and the PDP Research Group, Eds. Cambridge, MA: MIT Press, 1986, pp. 318–362.

[35] A. G. Bhatt, G. Kallianpur, and R. L. Karandikar, "Robustness of the nonlinear filter," *Stoch. Process. Their Appl.*, vol. 81, no. 2, pp. 247–254, Jun. 1999.

[36] K. Matsuoka, "Noise injection into inputs in back-propagation learning," *IEEE Trans. Syst. Man Cybern.*, vol. 22, no. 3, pp. 436–440, May/Jun. 1992.

[37] J. Qin Debnath, B. Bahrani, M. Saeedifard, and P. Barbosa, "Operation, control, and applications of the modular multilevel converter: A review," *IEEE Trans. Power Electron.*, vol. 30, no. 1, pp. 37–53, Jan. 2015.

[38] J. Kolb, F. Kammerer, and M. Braun, "Dimensioning and design of a modular multilevel converter for drive applications," in *Proc. 15th Int. Power Electron. Motion Control Conf.*, Sep. 2012, pp. LS1a–L1.1–1–LS1a–1.1–8.

Zheng Gong (Member, IEEE) received the B.Eng. degree in electrical engineering and automation and the Ph.D. degree in electrical engineering from China University of Mining and Technology, Xuzhou, China, in 2012 and 2017, respectively.

During 2015 to 2016, he was with the Department of Energy Technology, Aalborg University, Aalborg, Denmark, as a joint Ph.D. student. Since 2017, he has been with China University of Mining and Technology, where he is currently an Associate Professor with the School of Electrical Engineering. His research interests include the advanced topology and control for high-power converters, motor drives, renewable power generations, and high-voltage dc power transmissions.

Ping Tuo was born in Shaanxi, China, in 1999. He received the B.S. degree in electrical engineering, in 2021, from the China University of Mining and Technology, Xuzhou, China, where he is currently working toward the Ph.D. degree in electrical engineering.

His current research interests include model predictive control and multilevel converters.

Changming Zheng (Member, IEEE) received the B.Eng. degree in electrical engineering and automation and the Ph.D. degree in control theory and control engineering from China University of Petroleum (East China), Qingdao, China, in 2014 and 2020, respectively.

From 2018 to 2020, he has been a visiting Ph.D. student with the Department of Energy Technology, Aalborg University, Aalborg, Denmark. He is currently a Lecturer with the School of Electrical and Power Engineering, China University of Mining and Technology, Xuzhou, China, from 2021. His main research interests include model predictive control of power converters and PMSM drives.

Dr. Zheng was the recipient of the Best Student Paper Award at the 6th IEEE International Conference on Predictive Control of Electrical Drives and Power Electronics (PRECEDE) in 2021.

Xiaojie Wu (Member, IEEE) received the B.Eng. degree in industrial automation and the M.Sc. and Ph.D. degrees in electrical engineering from the China University of Mining and Technology, Xuzhou, China, in 1988, 1991, and 2000, respectively.

From 2002 to 2004, he was a Postdoctoral Research Fellow with Tsinghua University, Beijing, China. Since 2006, he has been a Professor with the School of Electrical and Power Engineering, China University of Mining and Technology. His research interests include advanced control of electrical drives and renewable energy generation systems.